

## Measurement of cross sections for electron capture into $n = 3$ states of hydrogen

M. C. Brower\* and F. M. Pipkin

*Lyman Laboratory, Harvard University, Cambridge, Massachusetts 02138*

(Received 19 September 1988)

We have measured the cross sections for electron capture into the  $n = 3, L, M_L$  states of hydrogen for protons colliding with helium atoms at energies between 30 and 80 keV. We used a microwave-resonance, optical detection technique, in which a microwave field drives transitions within the  $n = 3$  manifold of the hydrogen atoms, and the change in the Balmer- $\alpha$  light emitted in the decay of the excited atoms is observed. The analysis included cascade feeding of the  $n = 3$  states by higher  $n$  states. The measured cross sections decrease as the angular momentum  $L$  increases, and for fixed  $L$  they decrease as  $|M_L|$  increases. The  $3p$  and  $3d$  cross sections are roughly inversely proportional to the square of the energy over this range of energies, whereas the  $3s$  cross section peaks near 50 keV.

### I. INTRODUCTION

The process by which a proton captures an electron from an atom or molecule to form a ground- or excited-state hydrogen atom is relevant to a wide area of pure and applied physics. As a result, a great deal of effort has been devoted to measuring and calculating electron-capture cross sections.<sup>1-3</sup> However, research has paid comparatively little attention to the dependence of the cross sections on the orbital angular momentum  $L$  of the final state, and its projection on the axis of quantization  $M_L$ . Moreover, there are substantial discrepancies between some of the theoretical and experimental results which have been reported. In simple systems, the angular momentum dependence should provide a more definitive test of the theory and shed light on such processes as the post-collisional mixing of hydrogen states.<sup>4</sup>

This paper reports the measurements of cross sections for electron capture into  $n = 3, L, M_L$  hydrogen states formed in collisions of protons with helium atoms at energies between 30 and 80 keV. The experimental method is similar to one used initially to study electron capture into the  $n = 4$  states, and subsequently, the  $n = 3$  states from collisions of protons with nitrogen and hydrogen molecules.<sup>5-9</sup> The latter systems are too complex to be accessible to theory at present, but this is not true of protons colliding with helium.

Two other methods have been used to determine the partial cross sections for capture into the sublevels belonging to the  $n = 3$  manifold. Several groups have studied the light emitted by the hydrogen atoms as a function of position downstream from the collision cell and in some cases utilized the different lifetimes of the  $3s$ ,  $3p$ , and  $3d$  states to separate the signals from the three angular momentum levels.<sup>10-19</sup> These experiments determined the cross sections summed over  $M_L$  and did not give the partial cross sections for individual  $M_L$  levels. Risley and his co-workers<sup>20-23</sup> determined the axially symmetric density matrix for collisionally produced H ( $n = 3$ ) atoms by measuring the Stokes parameters which characterize the emitted Balmer- $\alpha$  radiation as a function

of axial and transverse electric fields applied in the collision cell. This experiment gives information on the partial cross sections for the individual  $M_L$  levels and the off-diagonal elements of the density matrix.

Three groups have reported calculations of the partial cross sections for capture into H ( $n = 3$ ). Winter and Lin<sup>24</sup> used the Born approximation and the method of close coupling to calculate the  $2s$ ,  $3s$ ,  $2p$ ,  $3p$ , and  $3d$  cross section for electron capture by protons in helium in the energy range 30–300 keV. Burgdörfer and Dubé<sup>25</sup> calculated the complete density matrix for the  $n = 3$  manifold of hydrogen coherently excited by electron capture in helium using the Born approximation including multiple scattering contributions and final-state interactions. Jain, Lin, and Fritsch<sup>26,27</sup> used the modified two-center atomic-orbital (AO) expansion method (denoted AO+) to calculate *ab initio* the differential and integrated (over impact parameters) density matrices of the excited hydrogen atoms in the  $n = 2$  and 3 manifolds formed in 25–100-keV proton-helium charge-transfer collisions.

This experiment incorporates two refinements on the original method which substantially reduce both systematic uncertainties and random uncertainties.<sup>5-9</sup> The first and most important refinement is to take more completely into account "cascade" feeding of the  $n = 3$  states by higher  $n$  states (mainly  $n = 4$ ) formed in the collisions. A byproduct of this analysis is an indirect measurement of the  $n = 4, L$  cross sections. We have found that cascade feeding strongly affects the populations of the short-lived  $3p$  and  $3d$  ( $L = 1, 2$ ) states. The reported experiments differ in the extent to which cascade feeding has been taken into account. This may account for some, though not all, of the discrepancies between the reported results.

The second refinement is to make measurements at two different distances between the collision cell and the microwave interaction region. This effectively doubles the number of independent data points.

Below we provide an overview of the method and analysis, followed by the method of calculating the theoretical signals, a description of the apparatus, the data analysis, discussion of the results, and conclusions.

## II. OVERVIEW OF THE METHOD

The main components of the experiments are depicted in Fig. 1. Protons in a monoenergetic beam capture electrons in collisions with helium atoms in a gas target. The resulting hydrogen atoms pass through a microwave-interaction region where a radio-frequency (rf) field drives transitions among the  $n=3$  states. After emerging from the rf region, the atoms pass in front of a photomultiplier tube equipped with an interference filter and optical linear polarizer, which detects Balmer- $\alpha$  radiation ( $n=3 \rightarrow 2$ ) emitted at right angles to the beam axis by the excited atoms. The beam current is monitored with a Faraday cup.

The experimental signal is the fractional change in the amount of light detected when the rf field is switched on and off,

$$S = \frac{N_{\text{off}} - N_{\text{on}}}{N_{\text{off}}} \quad (1)$$

The signal depends on the relative populations of the hydrogen states formed in the collisions and coupled by the rf field. Thus, it is the magnitude and sign of the resonance curves that is of interest in this experiment, rather than the center frequencies.

Figures 2 and 3 depict, respectively, the energy levels of the  $n=3$  and  $n=4$  hydrogen manifolds. We observe the signal over two frequency ranges, the first covering the  $3^2S_{1/2} \rightarrow 3^2P_{3/2}$  transition near 2940 MHz and the second the  $3^2P_{3/2} \rightarrow 3^2D_{5/2}$  transition near 1080 MHz. The latter transition is almost free of overlap from the  $3s \rightarrow 3p$  transition, and thus provides a very sensitive measure of the  $3p$  and  $3d$  cross sections. Near that frequency, however, there are small overlapping cascade signals from the  $4^2S_{1/2} \rightarrow 4^2P_{3/2}$  and  $4^2P_{1/2} \rightarrow 4^2D_{3/2}$  transitions near 1240 and 1370 MHz, respectively, due to atoms decaying into the  $n=3$  level after passing through the rf region. Two typical line scans, one from each frequency range, are shown in Figs. 4(a) and 4(b). The  $4^2S_{1/2} \rightarrow 4^2P_{3/2}$  cascade signal is clearly visible in Fig. 4(a).

Over each frequency range we vary the dependence of the signal on the cross sections by changing the distances between the target, the rf region, and the detector, and by rotating the rf electric field vector and the polarization axis of the optical polarizer. To determine the cross sec-

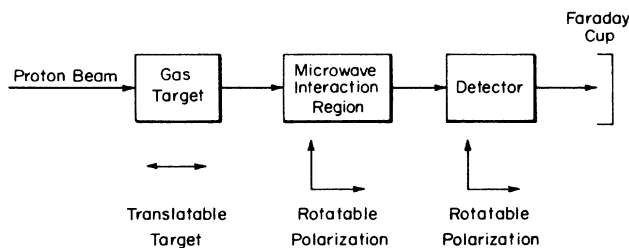


FIG. 1. Schematic diagram of the microwave-resonance optical-detection experiment used to study electron-capture collisions.

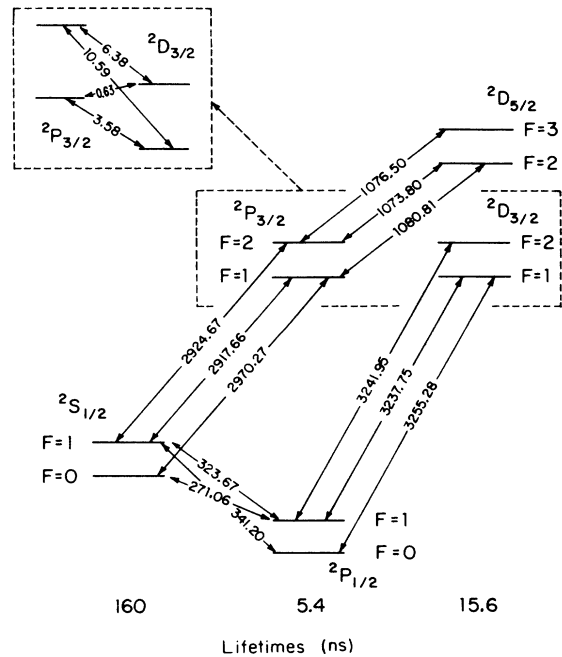


FIG. 2. Energy levels and allowed electric-dipole transitions for the  $n=3$  manifold of atomic hydrogen.

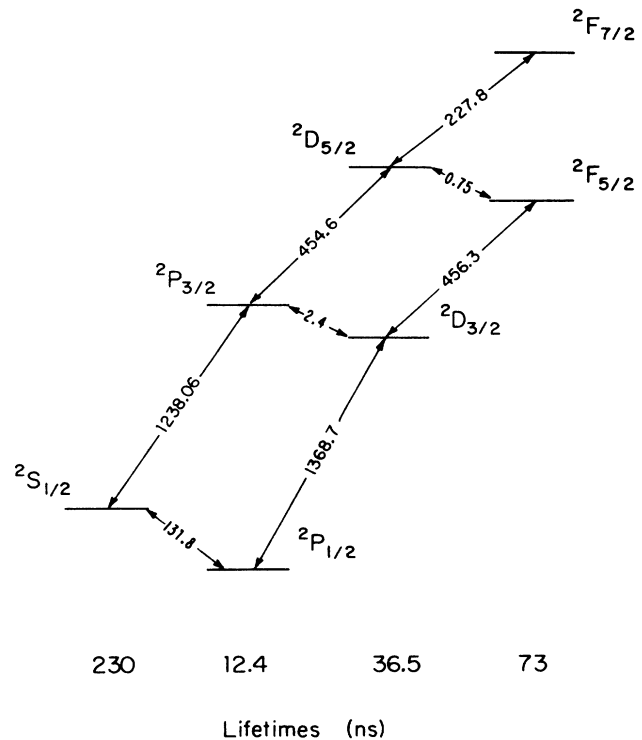


FIG. 3. Energy levels and allowed electric-dipole transitions for the  $n=4$  manifold of atomic hydrogen, excluding hyperfine structure.

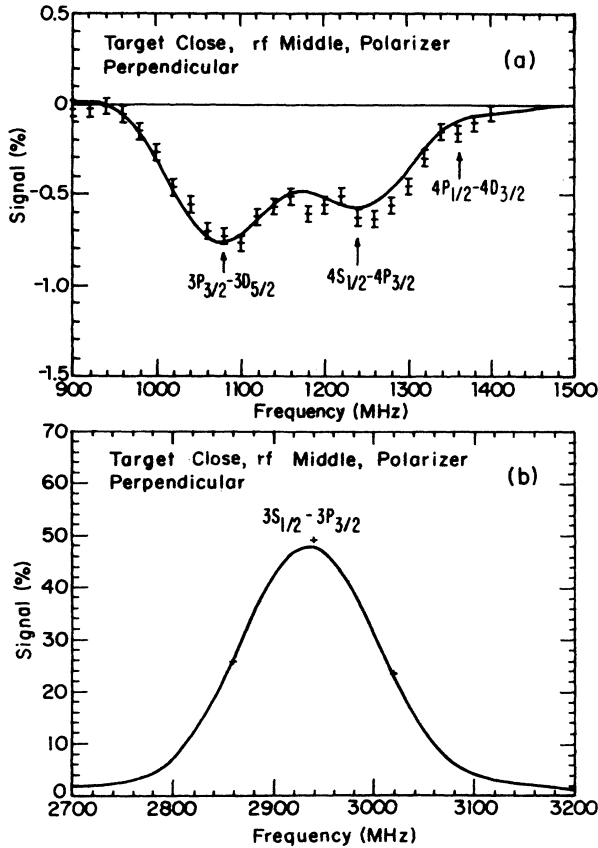


FIG. 4. Typical line scans. (a) The  $3^2P_{3/2} \rightarrow 3^2D_{5/2}$  transition near 1100 MHz. (b) the  $3^2S_{1/2} \rightarrow 3^2P_{3/2}$  transition near 2900 MHz. Also indicated in (a) are the transitions in the  $n=4$  states observed through cascades.

tions we fit the data to theoretical signals calculated for each state in each apparatus configuration. From the cascade signals we also deduce the  $n=4$  cross sections, and thus the amount of cascade feeding of the  $n=3$  states by the  $n=4$  states.

This method determines only the relative cross sections. The absolute cross sections are found separately from the photon counting rates, the detection efficiency, and the target pressure.

### III. THEORETICAL SIGNALS

At a given beam energy and rf frequency, the measured signal is the sum of the signals produced by the individual  $n, L, M_L$  states created in the collisions. Reversing the process—deducing the original populations from the measured signals—requires calculating theoretically the signals produced by atoms in any given initial state. The method of calculation is essentially the same as in Ref. 9, with the exception that states in levels higher than  $n=3$  (up to  $n=8$ ) are included. Here we describe briefly the basic method and discuss the new treatment of cascades.

The energy splittings between the hydrogen states are determined by the fine and hyperfine interactions. These interactions do not play a role in electron capture, however, because the collisional time scale is too short (on the

order of  $10^{-16}$  s). Therefore, the basic parameters characterizing the collisions are the cross sections for capture into the  $L, M_L$  states. These cross sections determine the initial populations of the fine and hyperfine states through well-known rules for coupling angular momenta. With the direction of the beam taken as the axis of quantization, symmetry requires that the cross sections not depend on the sign of  $M_L$ . With coherent excitation excluded, the number of independent parameters reduces to six cross sections for the  $n=3$  manifold and ten for the  $n=4$  manifold. For the cross sections we use the labels  $\sigma_{nL|M_L}$ , with the convention,

$$\sigma_{nL|M_L} = \sigma_{nLM_L} + \sigma_{nL-M_L}. \quad (2)$$

The density operator  $\rho$  completely describes the states. For the  $n=3$  manifold, several components of the density operator are defined. The first component  $\rho^{33}$  describes those atoms initially formed in the  $n=3$  state by electron capture. The other components,  $\rho^{3n}$  ( $n=4, 5, 6, 7, 8$ ), describe those atoms in the  $n=3$  state which were initially formed in higher  $n$  states and subsequently decayed to the  $n=3$  state; thus

$$\rho^3(t) = \rho^{33}(t) + \sum_{n=4}^8 \rho^{3n}(t). \quad (3)$$

The signals due to electron capture directly into the  $n=3$  level ( $\rho^{33}$ ) are calculated separately from the signals produced by the cascades ( $\rho^{3n}$ ). For the former, we include the hyperfine structure in  $\rho^{33}$  using the quantum numbers ( $n, S, L, J, F, M_F$ ). For the latter, the hyperfine structure is neglected to simplify the calculations, so that only the quantum numbers ( $n, S, L, J, M_J$ ) are used. Likewise the density operators for higher  $n$  levels,  $\rho^{nn}$ ,  $n > 3$ , include only the fine-structure states (as shown in the  $n=4$  energy-level diagram in Fig. 3). Secondary cascades (decays from higher  $n$  levels into  $n=3$  through one or more intermediate levels) are relatively unimportant and not considered here.

Experiments have indicated that electron capture creates coherent excitations among states of different  $L$ .<sup>22</sup> However, we cannot detect such coherences because the states involved decay to different final states, and the microwave field which mixes them destroys the coherent phases. The fine and hyperfine interactions, on the other hand, generate coherences which must, in principle, be included. In practice, the fine-structure energy splittings are so large that coherences between states of different  $J$  average to close to zero over the length of the gas target and the detection window. For that reason, only the hyperfine-induced coherences, which are restricted by symmetry to states of the same  $M_F$ , are incorporated in the density matrix,  $\rho^{33}(t=0)$ , created in the collisions.

#### A. $N=3$ signals

To calculate the theoretical  $n=3$  signals, we first postulate a population of one in a given  $n=3, L, M_L$  state formed in collisions, and calculate the resulting elements of the initial density operator  $\rho^{33}$  using angular-momentum coupling rules,<sup>28</sup>

$$\rho_{nLJFM_F}^{nLJF'M_F} = \sum_{M'_L, M'_S, M'_I, M_L, M_S, M_I} \langle F'M_F | J'IM'_J M'_I \rangle \langle J'IM'_J M'_I | L'IM'_L M'_S \rangle \times \delta_{LL'} \delta_{JJ'} \delta_{M_L M'_L} \delta_{M_S M'_S} \delta_{M_I M'_I} \langle LIM_L M_S | JIM_J M_I \rangle \langle JIM_J M_I | FM_F \rangle, \quad (4)$$

where

$$M_J = M_L + M_S = M_F - M_I,$$

$$M'_J = M'_L + M'_S = M_F - M'_I.$$

This equation allows only coherent excitations between states of the same  $L$ ,  $J$ , and  $M_F$ , but different  $F$ , as required.

After formation, the excited atoms traverse a field-free region where the density operator evolves according to the equation,

$$\rho^{33}(t) = \exp(-iE\Delta t) \rho^{33}(t_0) \exp(+iE^\dagger \Delta t). \quad (5)$$

In the Bethe-Lamb prescription,<sup>29</sup>  $E$  is the diagonal matrix of complex energies of the states (divided by  $\hbar$ ),

$$E_{\alpha\alpha} = \left[ \omega_\alpha - i \frac{\gamma_\alpha}{2} \right].$$

$\gamma_\alpha$  is the reciprocal of the lifetime of state  $\alpha$ , and  $\hbar\omega_\alpha$  is the energy of the state with respect to an arbitrary reference state. Explicitly,

$$\rho_{\alpha\beta}^{33}(t) = \rho_{\alpha\beta}^{33}(t_0) \exp[-(i\omega_{\alpha\beta} + \gamma_{\alpha\beta})\Delta t], \quad (6)$$

where

$$\omega_{\alpha\beta} = (\omega_\alpha - \omega_\beta), \quad \gamma_{\alpha\beta} = (\gamma_\alpha + \gamma_\beta)/2, \quad \Delta t = t - t_0.$$

Using Eq. (6), the initial density matrix is first averaged over the target pressure profile (described in a later section), then evolved from the target to the rf region. Inside the rf region, the rf field causes a dipole coupling between states. The Hamiltonian describing the atom-field interaction can be written as

$$H(t) = H_{\text{atom}} + H_{\text{field}} + H_{\text{int}}, \quad (7a)$$

where

$$H_{\text{int}} = 2\hat{V} \cos(\omega t + \phi), \quad (7b)$$

$$\hat{V} = -\frac{\mathbf{d} \cdot \mathbf{E}_0}{2} = -\frac{e\mathbf{r} \cdot \mathbf{E}_0}{2}. \quad (7c)$$

$H_{\text{atom}}$  is the complex Hamiltonian describing the atom and  $H_{\text{field}}$  is the Hamiltonian describing the radio-frequency field which we treat classically due to the large number of photons.  $H_{\text{int}}$  describes the interaction of this external field of amplitude  $\mathbf{E}$  with the atomic electric dipole moment  $\mathbf{d}$ .

The Schrödinger equation with this time-dependent Hamiltonian has no general analytic solution, but when the transition linewidth is small compared to the center frequency, a very good solution is obtained using the rotating-wave approximation, in which the nonresonant (called counter-rotating) term in  $\cos(\omega t + \phi)$  is discarded. The effective rf field amplitude is half its original amplitude. A unitary transformation removes the remaining time dependence from the Hamiltonian.

With the rf field amplitude constant, the time evolution of the density operator for the hydrogen atom is given by

$$\rho^{33}(t) = \exp(-iH\Delta t) \rho^{33}(t_0) \exp(+iH^\dagger \Delta t). \quad (8)$$

Since the actual rf field varies in amplitude and direction through the rf region, the time evolution is calculated using a number of steps of constant field amplitude. We find that 30 steps suffice for 0.1% accuracy.

The exponential in Eq. (8) is calculated by expansion in a Taylor series, and the desired degree of precision is obtained by extending the number of terms. The advantage of this method over the usual eigenvector method (used in Ref. 9) is that it is easier to apply in a computer program, and it requires no rotations of the density matrix when, as is generally the case, the rf field is not aligned with the axis of quantization. The disadvantage is that it takes more computing time. Only those few states resonantly coupled by the rf field must be included, however. The others evolve according to the field-free equations.

After the rf region the atoms again traverse a field-free region and pass in front of the detector window. The probability  $W$  of detecting a photon from the decay of atoms into the  $n=2$  level is

$$W = \frac{e^2 \omega^3}{\hbar c^3} \int_0^\infty \int_{\Delta\Omega(z')} dz' d\Omega \sum_{\substack{f, i, i' \\ \lambda, \lambda'}} \epsilon_{\lambda\lambda'}(\hat{\mathbf{p}}, \hat{\mathbf{k}}, z') \langle f | \mathbf{r} \cdot \hat{\mathbf{e}}_{\lambda'}^* | i \rangle \rho_{ii}^{33}(t') \langle i' | \mathbf{r} \cdot \hat{\mathbf{e}}_\lambda | f \rangle, \quad (9)$$

where

$$t' = z'/v.$$

In this expression  $i, i'$  are the initial ( $n=3$ ) states and  $f$  the final ( $n=2$ ) state.  $\epsilon_{\lambda\lambda'}(\hat{\mathbf{p}}, \hat{\mathbf{k}}, z')$  is the efficiency matrix,

discussed in depth in Ref. 9, for detecting a linearly polarized photon emitted at  $z'$  in a propagation direction  $\hat{\mathbf{k}}$  with the optical polarizer set to transmit photons with a polarization vector  $\hat{\mathbf{p}}$ .  $\epsilon_{\lambda\lambda'}$  incorporates the transmission efficiencies of the interference filter and optical polarizer and the detection efficiency of the photomultiplier tube.

It also includes a "polarization mixing factor"  $B(z')$ , discussed below, which determines the mix of photon polarizations detected from  $\Delta M_F = \pm 1$  decays due to the nonzero detection solid angle,  $\Delta\Omega(z')$ . The integral over  $z'$  is approximated by summing the integrand across the detector window in 18 steps of constant detection efficiency.  $v$  is the velocity of the atoms in the beam and  $t'$  the distance along the beam line.

The theoretical probability of detecting a photon,  $A_{3L|M_L}(\omega, \mathbf{E}, \delta)$ , due to an atom originally in the  $n=3, L, |M_L\rangle$  state (initial population one) is calculated from the detection probability  $W$ ,

$$A_{3L|M_L}(\omega, \mathbf{E}, \delta) = W(\omega, \mathbf{E}, \delta). \quad (10)$$

$\omega$  and  $\mathbf{E}$  are the frequency and peak field strength, respectively, of the rf field, and  $\delta$  is the angle between the transmission axis of the optical polarizer and the quantization (beam) axis.

### B. Cascade signals

Cascade signals come from one of three sources: (1) atoms which decay into the  $n=3$  level before the rf region; (2) atoms which decay into the  $n=3$  level in the rf region; and (3) atoms which decay into the  $n=3$  level after the rf region and after undergoing transitions driven by the rf field. The third type is the most visible [see Fig. 4(a)] but the first is actually the most important, since it affects the relevant  $n=3$  populations before the atoms reach the rf region. After a distance of a few centimeters decays from the  $4s$  state into the  $3p$  state dominate the  $3p$  populations remaining from the collisions, despite the long lifetime of the  $4s$  state. The systematic errors that could result from ignoring this effect were not fully appreciated in our earlier efforts to measure electron-capture cross sections (Refs. 5–9).

The  $n=4$  level is the largest contributor of cascades. To account for it, we use the observed  $4^2S_{1/2} \rightarrow 4^2P_{3/2}$  and  $4^2P_{1/2} \rightarrow 4^2D_{3/2}$  cascade signals to determine the  $n=4$  cross sections while at the same time we determine the  $n=3$  cross sections from the  $n=3$  signals. This requires calculating the theoretical signal produced by atoms in any given  $n=4, L, M_L$  state. As noted earlier, in these calculations only the fine structure of the  $n=3$  and  $n=4$  levels are included. This reduces the 100-MHz effective linewidth of the  $3^2P_{3/2} \rightarrow 3^2D_{5/2}$  transition by 7 MHz and the cascade signals by somewhat less. This is a small effect compared to the statistical uncertainties in the signals, and is therefore ignored.

In the field-free regions, the time evolution of  $\rho^{44}$ , which describes the  $n=4$  states, is given by

$$\rho_{ii'}^{44}(t) = \rho_{ii'}^{44}(t_0) \exp[-(i\omega_{ii'} + \gamma_{ii'})\Delta t]. \quad (11a)$$

The rate of change of  $\rho^{34}$ , which describes the  $n=3$  states created by decays from the  $n=4$  level, is given by

$$\frac{\partial \rho_{ff'}^{34}}{\partial t} = -(i\omega_{ff'} + \gamma_{ff'})\rho_{ff'}^{34}(t) + \sum_{ii'} W_{ff'ii'} \rho_{ii'}^{44}(t). \quad (11b)$$

In these expressions  $f, f'$  and  $i, i'$  refer, respectively, to  $n=3$  and  $n=4$  states; and  $\omega_{ff'}$ ,  $\omega_{ii'}$ ,  $\gamma_{ff'}$ , and  $\gamma_{ii'}$  are as defined in Eq. (6).  $W_{ff'ii'}$  is the rate of decay of states from  $n=4$  into  $n=3$ , given by

$$W_{ff'ii'} = \frac{e^2 \omega^3}{\hbar c^3} \int_{4\pi} d\Omega \sum_{\lambda\lambda'} \langle f | \mathbf{r} \cdot \hat{\mathbf{e}}_\lambda^* | i \rangle \times \langle i' | \mathbf{r} \cdot \hat{\mathbf{e}}_{\lambda'} | f \rangle. \quad (11c)$$

With the substitutions

$$\Omega_{ff'} = -(i\omega_{ff'} + \gamma_{ff'}), \quad \Omega_{ii'} = -(i\omega_{ii'} + \gamma_{ii'}),$$

the solution for the time evolution of  $\rho^{34}(t)$  is

$$\begin{aligned} \rho_{ff'}^{34}(t) &= \rho_{ff'}^{34}(t_0) \exp(\Omega_{ff'} \Delta t) \\ &+ \frac{W_{ff'ii'}}{\Omega_{ff'} - \Omega_{ii'}} \rho_{ii'}^{44}(t_0) \\ &\times [\exp(\Omega_{ff'} \Delta t) - \exp(\Omega_{ii'} \Delta t)]. \end{aligned} \quad (11d)$$

If  $t_0$  is chosen to be the time of collision, then  $\rho^{34}(t_0) = 0$ .

In the rf region, Eq. (8) is adapted to evolve the  $n=3$  and  $n=4$  density operators ( $\rho^{34}$  and  $\rho^{44}$ ) independently over each constant-field step and Eq. (11b) is used to add cascade feeding to  $\rho_{34}$  at the end of each step. We find, as before, that 30 steps provide adequate accuracy. Equation (9) gives the probability of photon detection over each of the 18 steps across the detector window, with  $\rho^{34}$ , given by Eq. (11d), substituted for  $\rho^{33}$ .

We also take into account cascades from  $n$  levels higher than  $n=4$ . Since the corresponding cascade signals are difficult to observe, it is necessary to estimate the populations of these states from other considerations. The Born approximation predicts<sup>1</sup> that the electron-capture cross sections for the  $s$  states decrease as  $1/n^3$ . We assume, therefore, that the population of each state in  $n=5, 6, 7, 8$  ( $L=0, 1, 2, 3$  only) is initially a factor of  $(4/n)^3$  lower than the equivalent state in the  $n=4$  manifold. The populations of states with  $L > 3$  are assumed to be zero. The cascade contributions of the  $n > 4$  states are included automatically when the  $n=4$  cascade signals are calculated. Thus the only free parameters in the calculations of the total cascade signals are the initial populations of the  $n=4$  states. The cascade contribution of  $n > 4$  states is typically one-third that of the  $n=4$  states.

## IV. APPARATUS

The apparatus, shown in Fig. 5, is similar to that used in Ref. 9, with two important changes: the gas target has been redesigned to improve its isolation from the vacuum system; and the target has been placed on a track to allow

it to move with respect to the detector and the rf region. In addition, our understanding of the dependence of the detection efficiency on emission angle and position along the beam line has improved. Here we describe the apparatus briefly, placing emphasis on the changes. The important apparatus dimensions are shown in Table I, and the operating conditions at each beam energy are summarized in Table II.

The proton beam is generated by a commercial radio-frequency ion source. The protons are extracted, focused, and then accelerated in a high-voltage column. After leaving the accelerator, the beam passes through an electrostatic quadrupole, 30° horizontal bending magnet, a second quadrupole, and a pair of balanced vertical electrostatic deflection plates. This arrangement focuses and steers the beam and separates protons from the molecular ions  $H_2^+$  and  $H_3^+$ . Two circular apertures before the target collimate the beam to a diameter of 1.5 mm through the target, 2 mm through the rf region, and 2.5 mm through the detection region; the beam touches no apertures after collimation. All components are optically aligned to 0.3 mm. The proton current entering the target is maintained at  $8 \mu A$  ( $\pm 1 \mu A$ ). The beam energy is determined from the accelerating potential to within  $\pm 1$  kV. Helmholtz coils surrounding the apparatus reduce the magnetic field between the target and the detector to less than 20 mG. Three diffusion pumps keep the beam line at a pressure of  $3 \times 10^{-7}$  torr or less and a fourth diffusion pump is devoted to the target alone.

The main gas target, 1.425 cm in length, moves on a track between two positions separated by 1.27 cm along the beam axis. An Alphasatron ionization gauge monitors the gas-feed line pressure, which is in turn calibrated by a Baratron capacitance manometer inserted directly into the target. Computer-controlled solenoid valves on the gas-feed line switch the gas flow to the target on and off, so that during the data runs the data-taking computer can record the signal from collisions with background gas in the system. Such collisions account for about 10% of the neutral beam atoms when the target is on (for target pressures shown in Table II).

TABLE I. The important dimensions of the apparatus, in centimeters.

Beam diameter	0.15–0.25
Main target length	1.425
Target to rf region	1.854–4.993
rf region	4.089–4.445
rf region to detector	4.447–6.317
Detector window	3.353
Total target to detector	12.260–13.530

Gas leaking out of the target into the vacuum system is a second source of background signal which cannot be measured by turning the target off. With the single-chamber target design used in earlier work, leakage accounted for about 20% of the neutral beam atoms when the target was on. This was difficult to account for accurately and significantly reduced the sensitivity of the experiment to the short-lived  $3p$  and  $3d$  states. As a result, we have adopted an improved target design with buffer regions placed just before and just after the main target, 1.39 and 1.00 cm in length, respectively, and pumped independently from the rest of the vacuum system. Figure 6 shows the target assembly. The resulting gas leakage creates about 3% of the neutral atoms in the beam, which is small enough to be ignored. The gas pressure in the buffer regions, calculated from gas-flow equations to be about 13% of the pressure in the main target, is included in the pressure profile of the target in calculating the theoretical signals.

The percent beam neutralization by the target depends on the target gas pressure and the cross sections for charge capture into all  $n$  levels of hydrogen. The value calculated using measured cross sections in the literature<sup>30</sup> is less than 3% over the range of operating pressures and energies, and agrees with the measured value (Table II) within experimental uncertainties. The linear dependence of detected radiation on target gas pressure indicates that multiple collisions are unimportant.

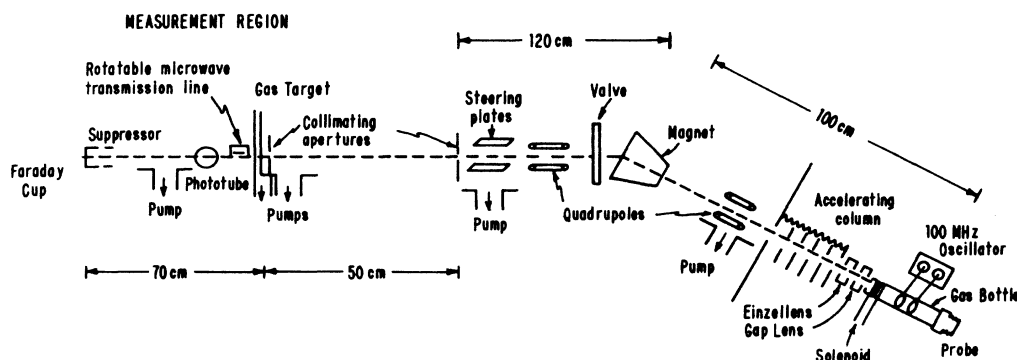


FIG. 5. A schematic diagram of the apparatus showing the accelerator and the beam line.

TABLE II. A summary of the operating conditions for each of the four energies at which data were taken.  $N/I$  is the ratio of the counting rate in the photomultiplier tube to the beam current with the rf field off. Values in parentheses denote the estimated uncertainty in the last digit.

Energy (keV)	30(1)	50(1)	60(1)	80(1)
Beam current ( $\mu\text{A}$ )	8(1)	8(1)	8(1)	8(1)
Target pressure (mTorr)	2.5(2)	2.1(1)	2.0(1)	3.7(2)
Estimated beam neutralization (%)	2.7	1.4	1.1	1.0
Nominal rf power (mW)	400	400	400	400
Typical $N/I$ (target on)	1.68	1.70	1.36	1.52
Typical $N/I$ (target off)	0.19	0.16	0.15	0.14
Uncertainty in signal based on observed scatter (0.01%)	3.7	4.7	4.1	3.6

The rf region is a rectangular coaxial transmission line with slots cut in the outer walls and the center conductor for the beam to pass through.<sup>9</sup> It can be rotated through  $360^\circ$  while the system is under vacuum. The axis of rotation is off center, so that the target-rf region distance changes. There are four possible orientations of the rf region which allow the beam to pass through—one close to the target, one far from the target, and two in the middle. The two middle orientations are experimentally indistinguishable, so only one is used, resulting in three independent positions in all. In the close and far positions the dominant direction of the rf electric-field vector is parallel to the beam axis; in the middle position it is perpendicular.

The detector observes the beam through a circular window 3.35 cm in diameter. The axis of the linear polarizer behind the window is oriented either parallel or perpendicular to the beam axis. The 100-nm-bandwidth interference filter is centered on the Balmer- $\alpha$  wavelength (656 nm). A thermocouple cools the RCA 8852 photomultiplier tube to  $-20^\circ\text{C}$  to reduce thermal noise. The large size of the photomultiplier housing requires the face

of the photomultiplier tube to be pulled back 28 cm from the beam line and connected to the window through a tube 5 cm in diameter. A lens and reflective aluminized Mylar in the tube partially compensate for the resulting decrease in the detection solid angle. The overall detection efficiency, including the measured quantum efficiency of the photomultiplier tube and the average detection solid angle, is  $2.5(5) \times 10^{-4}$ . The largest source of uncertainty is the effective frontal area of the photomultiplier tube.

The relative detection efficiency is measured at each of 18 steps by moving a small light source across the field of view. We find, as expected, that the detection efficiency peaks sharply at the center because of the lens. This reduces the detectability of the short-lived  $3p$  and  $3d$  states compared to the  $3s$  state. The average angle of detection is likewise measured by inserting apertures in front of the detector while the light source is moved. This angle influences the polarization of light detected from decays in which  $\Delta M_F = \pm 1$ . (Decays with  $\Delta M_F = 0$  are unaffected). If one uses the spherical coordinates  $\theta$  and  $\phi$  with the beam axis as the  $z$  axis to describe the direction  $\mathbf{k}$  of propagation of the emitted photon, the light is elliptically polarized with the fraction  $\cos^2\theta/2$  polarized in the  $kz$  plane and the fraction  $\frac{1}{2}$  polarized perpendicular to the  $kz$  plane. The average polarization mix over the solid angle of detection is expressed as a mixing factor, given by

$$B(z') = \frac{\int_{\Delta\Omega(z')} \cos^2\theta d\Omega}{\Delta\Omega(z')} \quad (12)$$

For radiation emitted at right angles to the beam  $B(z')=0$ . The measured value of  $B(z')$  reaches a peak of 0.10 near the edge of the field of view, and falls to 0.06 at the center.

An IBM PC computer controls the experiment. Voltage-to-frequency converters convert the Faraday cup (beam current) and rf power-meter voltages to trains of TTL pulses, which, together with the photomultiplier pulses, are integrated by counters. For a single point at a given rf frequency, a clock switches the rf power on and off at 8 Hz over a 64-sec period. The counters are gated

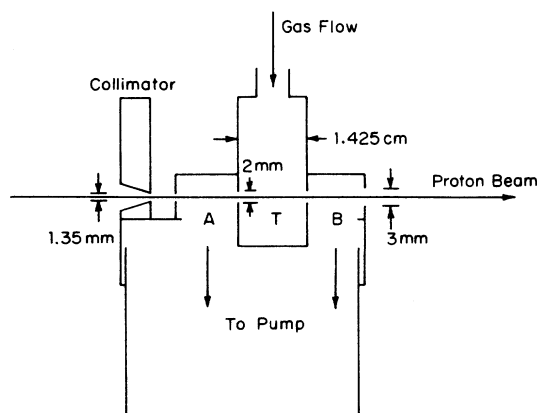


FIG. 6. A diagram of the buffered gas target used to reduce gas leakage into the vacuum system.

by the clock to count in only one of the two rf states (on or off). The computer records the accumulated number of photon counts  $N$  in each rf state, corrects for the dead time of the counting circuits, divides the result by the beam current  $I$  to eliminate the effect of current drifts, then calculates the signal. At each rf frequency, the computer records six points with the target on and two with the target off and uses the results to calculate the corrected signal with the background removed. Based on the number of photon counts per point, the expected Poisson uncertainty in the net signal (corrected for the signal with the target off) is  $4 \times 10^{-4}$ , in good agreement with the observed scatter of the signals (Table II).

$$S(\omega, \mathbf{E}, \delta) = \frac{\sum_{\substack{L, M_L \\ n=3,4}} \sigma_{nL|M_L} [A_{nL|M_L}(\omega, \mathbf{0}, \delta) - A_{nL|M_L}(\omega, \mathbf{E}, \delta)]}{\sum_{\substack{L, M_L \\ n=3,4}} \sigma_{nL|M_L} A_{nL|M_L}(\omega, \mathbf{0}, \delta)} \quad (14)$$

The 12 quasi-independent configurations of the apparatus (two directions of the rf electric field, two directions of the optical polarizer axis, three distances between the target, rf region, and detector), combined with the two fre-

## V. DATA ANALYSIS

The measured signal is defined as the fractional change in the observed light (corrected for background) when the microwave field is switched on,

$$S(\omega, \mathbf{E}, \delta) = [N(0, \mathbf{0}, \delta) - N(\omega, \mathbf{E}, \delta)] / N(0, \mathbf{0}, \delta), \quad (13)$$

where  $N(0, \mathbf{0}, \delta)$  is the photon count rate when the rf field is off, and  $N(\omega, \mathbf{E}, \delta)$  is the photon count rate when the rf field is on. This signal can be expressed in terms of the detection probability derived earlier for each  $n, L, |M_L|$  state ( $n = 3, 4$ ),

quency ranges observed, provide enough independent data to invert this equation, and determine the  $n = 3, L, |M_L|$  cross sections, normalized to  $\sigma_{300}$ . In addition, the  $n = 4, L$  cross sections ( $L = 0, 1, 2$ ) can also be

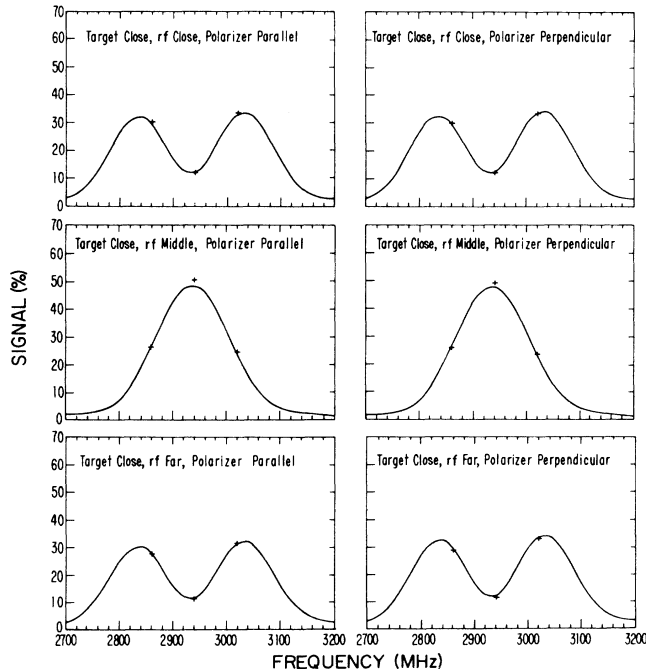


FIG. 7. Line scans at 50 keV for the  $3^2S_{1/2} - 3^2P_{3/2}$  transition, with the target close to the rf region. Parallel and perpendicular polarizations refer to the alignment of the optical polarizer axis with the beam axis. rf close, middle, and far refer to the position of the rf region with respect to the target. For the close and far positions the rf electric field is parallel to the beam axis; for the middle position the rf electric field is perpendicular to the beam axis.

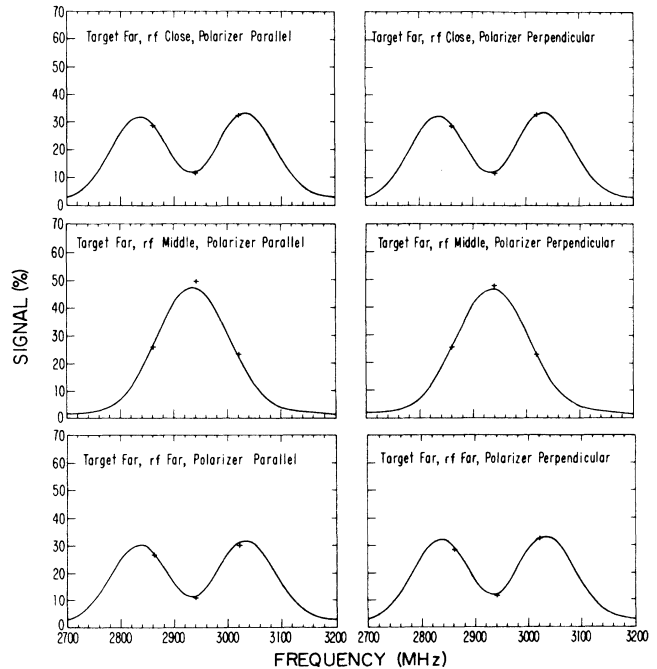


FIG. 8. Line scans at 50 keV for the  $3^2S_{1/2} - 3^2P_{3/2}$  transition with the target far from the rf region. Parallel and perpendicular polarizations refer to the alignment of the optical polarizer axis with the beam axis. rf close, middle, and far refer to the position of the rf region with respect to the target. For the close and far positions the rf electric field is parallel to the beam axis; for the middle position the rf electric field is perpendicular to the beam axis.

found, although as discussed below there is not enough information to determine their  $M_L$  dependence. A linear least-squares-fitting procedure is used to fit the data. The statistical uncertainties in the results represent the change in each cross section that would cause an increase of one in  $\chi^2$ . Figures 7–10 show all the fits used to determine the cross sections at an energy of 50 keV.

Certain constraints make it necessary to iterate the linear least-squares procedure until the cross sections converge. We describe these constraints below.

#### A. $n = 3$ cross sections

The  $3s$  cross section dominates the signals in the 2860–3020-MHz range, whereas the  $3p$  and  $3d$  cross sections dominate in the 900–1400 MHz range. As a result, the latter range is better suited to determining the  $p$  and  $d$  cross sections, while the former is better suited to determining the  $s$  cross section. The fit is therefore alternated between frequency ranges, with  $3s$  fixed in the 900–1400 MHz range, and  $3p$  and  $3d$  fixed in the 2860–3020 MHz range, until the cross sections converge. This generally requires two iterations.

#### B. $n = 4$ cross sections

The  $n = 4$  cascade signals we observe are one to two orders of magnitude smaller than the signals from the

equivalent  $n = 3$  states. As a result, the measured  $4p$ ,  $4d$ , and  $4f$  cross sections are strongly influenced by systematic effects and tend to assume physically unreasonable values if they are entirely unconstrained in the fit. The effect on the  $n = 3$  cross sections is small, however, since the  $4s$  state, which dominates the cascade feeding, is relatively immune to this problem.

The method of constraint we have chosen is to fix the  $n = 4, L, |M_L| \neq 0$  cross sections in the same ratio to the  $n = 4, L, M_L = 0$  cross sections as the equivalent cross sections in  $n = 3$ ; that is,

$$\frac{\sigma_{411}}{\sigma_{410}} = \frac{\sigma_{311}}{\sigma_{310}}, \quad \frac{\sigma_{421}}{\sigma_{420}} = \frac{\sigma_{321}}{\sigma_{320}}, \quad \frac{\sigma_{422}}{\sigma_{420}} = \frac{\sigma_{322}}{\sigma_{320}}. \quad (15)$$

The total cross sections (summed over  $M_L$ ) are unconstrained. In addition, the  $4f$  total cross section is constrained to be in the same ratio to the  $4d$  total cross section as the  $3d$  total cross section is to the  $3p$ . The dependence of the  $4f$  cross sections on  $M_L$  is fixed through a rough extrapolation of the relationships found among the  $3d$  and  $3d$  states,

$$\sigma_{431} = \sigma_{430}, \quad \sigma_{432} = \sigma_{430}/4, \quad \sigma_{433} = \sigma_{430}/8. \quad (16)$$

Up to 20 iterations of the fit are required to arrive at a converged solution. We have used widely different initial cross sections and the final results are the same. In addition, we have used different relationships among the

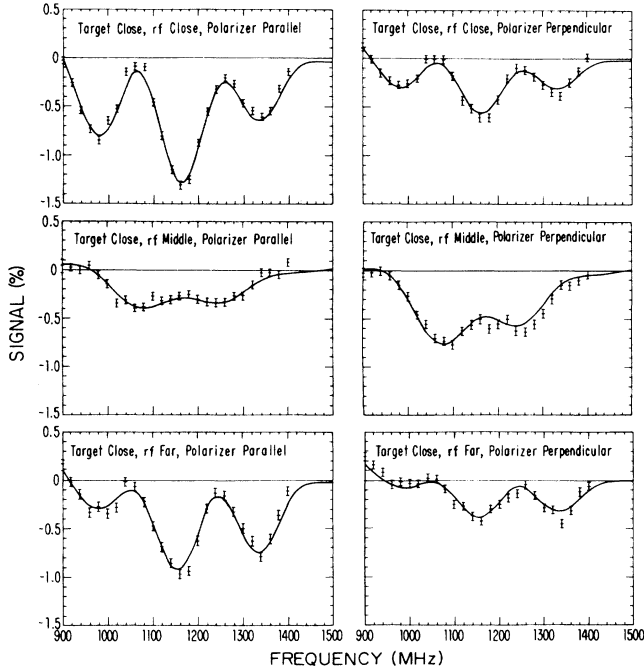


FIG. 9. Line scans at 50 keV for the  $3^2P_{3/2} - 3^2D_{5/2}$  transition with the target close to the rf region. Parallel and perpendicular polarizations refer to the alignment of the optical polarizer axis with the beam axis. rf close, middle, and far refer to the position of the rf region with respect to the target. For the close and far positions the rf electric field is parallel to the beam axis; for the middle position the rf electric field is perpendicular to the beam axis.

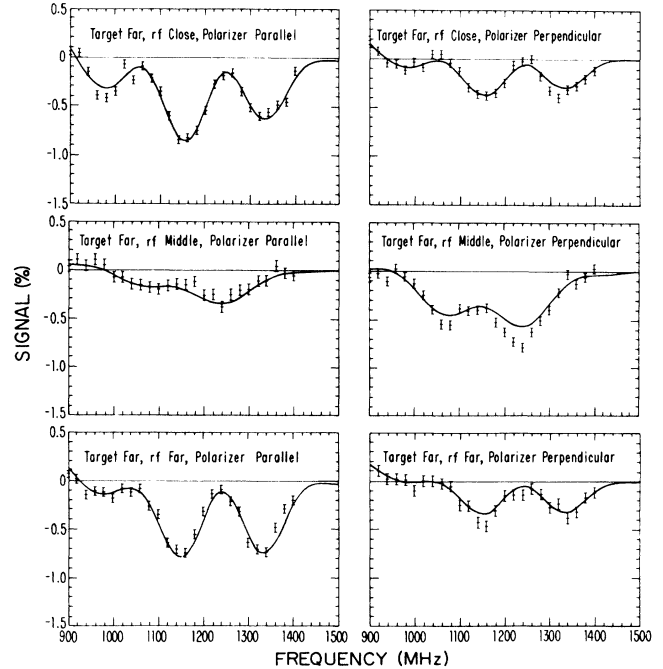


FIG. 10. Line scans at 50 keV for the  $3^2P_{3/2} - 3^2D_{5/2}$  transition with the target far from the rf region. Parallel and perpendicular polarizations refer to the alignment of the optical polarizer with the beam axis. rf close, middle, and far refer to the position of the rf region with respect to the target. For the close and far positions the rf electric field is parallel to the beam axis; for the middle position the rf electric field is perpendicular to the beam axis.

$n=4$  states and concluded that the effect on the  $n=3$  cross sections is within experimental uncertainties.

### C. Absolute cross sections

At each energy the  $3^2S_{1/2} \rightarrow 3^2P_{3/2}$  signals are used in combination with the pressure profile of the target, the beam current, the photon-counting rate, and the overall detection efficiency to determine the absolute cross section  $\sigma_{300}$ . The overall uncertainty in  $\sigma_{300}$ , due largely to uncertainties in the detection efficiency and target pressure, is estimated to be 20%. However, the relative uncertainty in the cross section from one energy to the next is less than 5%.

### D. Systematic effects

The most troublesome potential source of systematic error is the interaction of atoms with protons in the beam or with electric fields from charge built up on surfaces near the beam. These interactions could mix nearly degenerate states in  $n=3$  and higher levels. Their importance in our experiment is difficult to judge. One simple gauge is the root-mean-square electric field produced by protons in the beam. At our beam current of  $8\mu\text{A}$ , this field is estimated to be 0.25 V/cm, assuming neutralizing electrons and negative ions are absent. This is to be compared with the critical values for mixing various states,<sup>29</sup>

$n$	$^2S_{1/2} \rightarrow ^2P_{1/2}$ (V/cm)	$^2P_{3/2} \rightarrow ^2D_{3/2}$ (V/cm)
3	23.7	2.85
4	4.9	0.70
5	1.6	0.25
6	0.7	0.09

Clearly the postulated proton field should not mix  $n=3$  or  $n=4$  states significantly, but could have a significant effect on states in higher levels.

Our measurements of the variation of the signals with beam current tend to support this conclusion. For beam currents ranging from 5 to 14  $\mu\text{A}$  there is no observable change in the  $4^2S_{1/2} \rightarrow 4^2P_{3/2}$  cascade signal and the  $3^2P_{3/2} \rightarrow 3^2D_{5/2}$  signal decreases by less than 10%. The decrease does not necessarily indicate mixing of the  $n=3$  states, but could be from mixing of  $n=4$  and higher states before they decay into the  $n=3$  level.

Nevertheless, we are unable to obtain good fits of the signals in the 900–1400-MHz range in some twelve apparatus configurations (see Figs. 9 and 10). This may be due to the different effects of electric fields in the various configurations.

## VI. RESULTS AND DISCUSSION

Table III summarizes our results. In addition to the  $n=3, L, |M_L|$  cross sections, the  $n=4, L$  cross sections, summed over  $M_L$ , are listed up to  $L=2$ . The quoted  $\chi^2/\mathcal{D}$  ( $\chi^2$  divided by the number of degrees of freedom,  $\mathcal{D}$ ) is over the 900–1400-MHz range only. Over the 2860–3020-MHz range it is larger, indicating the presence of systematic errors on the order of 1–2% of the signal (insignificant in the low-frequency range where the statistical scatter is larger in relation to the signals). These errors are probably the result of imperfect rf-power corrections for reflections from the rf components.

The uncertainties in the relative cross sections range from 10% to 20% for  $\sigma_{310,1}$  and from 20% to 30% for  $\sigma_{320,1,2}$ . As noted earlier, the systematic uncertainty in the absolute cross section  $\sigma_{300}$  to which the others are normalized, is about 20%, although the relative uncertainties between energies are less than 5%.

### A. Comparison with other experiments and theory

Figure 11 shows a plot of the cross sections measured in this experiment together with the recent calculations

TABLE III. Results for  $N=3$  and  $N=4$  cross sections. Values in parentheses denote one standard deviation uncertainties.

Cross section	Energy (keV)			
	30	50	60	80
$\sigma_{300}(\pm 20\%)$ ( $10^{-18} \text{ cm}^2$ )	1.6	2.4	2.0	1.4
$\sigma_{300}$	1	1	1	1
$\sigma_{310}$	0.58(8)	0.19(2)	0.18(2)	0.13(1)
$\sigma_{311}$	0.36(6)	0.08(1)	0.04(1)	0.05(1)
Total	0.94(10)	0.27(2)	0.22(2)	0.18(1)
$\sigma_{320}$	0.055(10)	0.017(4)	0.019(4)	0.013(3)
$\sigma_{321}$	0.046(7)	0.014(3)	0.014(3)	0.010(2)
$\sigma_{322}$	0.022(4)	0.001(2)	0.002(2)	-0.002(2)
Total	0.123(12)	0.032(5)	0.031(5)	0.021(4)
$\sigma_{400}$	0.24(1)	0.46(1)	0.55(1)	0.54(1)
$\sigma_{41}$ (Total)	0.93(7)	0.21(3)	0.43(4)	0.31(3)
$\sigma_{42}$ (Total)	0.14(3)	0.05(2)	0.07(2)	0.04(2)
$\chi^2/\mathcal{D}$	4.1	1.6	2.8	3.0

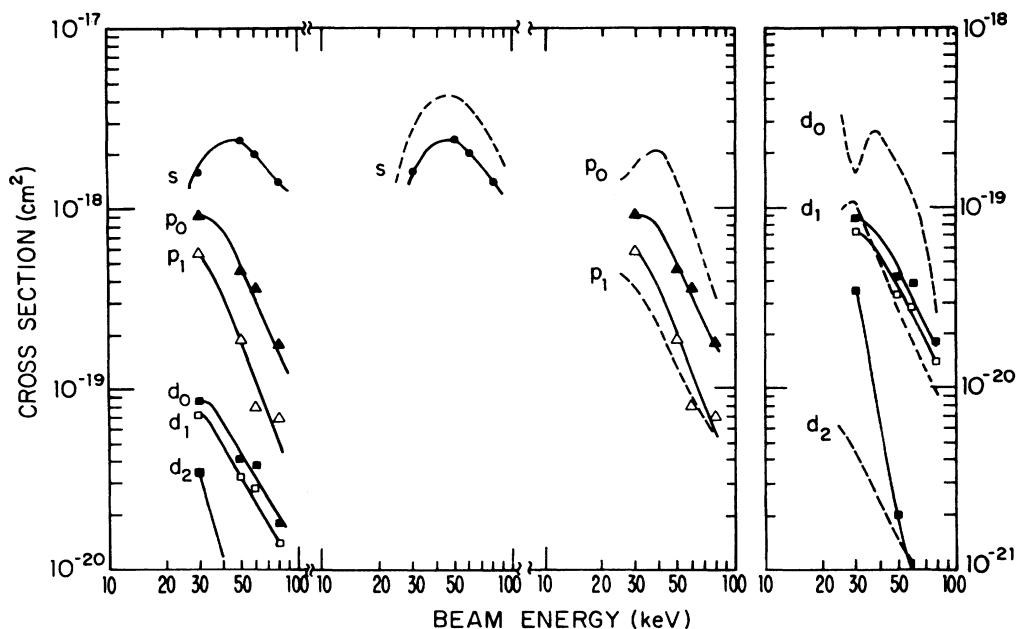


FIG. 11. Results of our experiment for  $n=3$  compared with the atomic orbital calculations of Jain, Lin, and Fritsch (Ref. 27). The points are the measured cross sections; the solid lines are curves through the measured points to guide the eye; the dashed curves are the theoretical predictions.

of Jain, Lin, and Fritsch.<sup>27</sup> The plotted cross sections are the summed cross sections given by Eq. (2). Care must be taken when comparing results because this convention is not always used. There are obvious discrepancies between our results for  $n=3$  and the atomic orbital (AO+) calculations of Jain, Lin, and Fritsch. The calculated  $3s$  cross section, in particular, is up to twice as large as the measured value, and the calculated cross sections decline more quickly with  $M_L$ . This type of calculation should be accurate over this range of energies since it includes molecular-orbital effects in the collisions.

Table IV shows a comparison of our results at 60 keV with those of Westerveld *et al.*<sup>23</sup> Westerveld and his co-workers measured the relative electron-capture cross sections, but not the absolute cross section  $\sigma_{300}$ . Their ex-

TABLE IV. Comparison of the results of this experiment at 60 keV with the measurements of Westerveld *et al.* (Ref. 23).

	This experiment	Ref. 23	
		a	b
$\sigma_{300}$	1	1	1
$\sigma_{310}$	0.18(2)	0.21(4)	0.25(5)
$\sigma_{311}$	0.04(1)	0.06(2)	-0.02(2)
Total	0.22(2)	0.27(4)	0.23(5)
$\sigma_{320}$	0.019(4)	0.06(5)	0.01(6)
$\sigma_{321}$	0.014(3)	-0.04(8)	0.01(2)
$\sigma_{322}$	-0.002(2)	0.02(2)	0.01(1)
Total	0.031(5)	0.04(10)	0.03(6)

<sup>a</sup>Axial electric field.

<sup>b</sup>Transverse electric field.

periment subjects the atoms to a static electric field inside the target and observes Balmer- $\alpha$  radiation emitted as a function of electric-field strength and circular optical polarization. They are primarily interested in measuring the collision-induced coherences among the states rather than the diagonal cross sections. Table IV shows that their  $3p$  cross sections are consistent with ours, but comparison of the  $3d$  cross sections is inconclusive because their uncertainties are comparable to their cross sections.

A larger number of theoretical and experimental results are available for cross sections summed over  $M_L$ . Figure 12 compares our results with three other experiments and two theoretical calculations. Hughes *et al.*,<sup>12</sup> Ford and Thomas,<sup>14</sup> and Lenormand<sup>17</sup> all deduced the cross sections from the change in intensity of Balmer- $\alpha$  light emitted by the atoms over some distance after the gas target (and in Lenormand's experiment, inside the target as well). They quote uncertainties of 10–25%.

The agreement between our results and Lenormand's is excellent for the  $3s$  and  $3p$  cross sections, and is within the combined experimental uncertainties for the  $3d$  cross sections. Hughes *et al.*, on the other hand, sharply disagree. For  $3s$ , the discrepancy between their results and ours grows to 50% at 30 keV. Their  $3p$  cross sections are up to a factor of 3 lower than ours at higher energies, while their  $3d$  cross sections are up to a factor of 2 larger than ours. Furthermore, the dependence of all cross sections on energy is quite different. Possible errors in the detection efficiency or the target pressure in any of the experiments cannot account for all of the discrepancies. It is difficult to draw conclusions from Ford and Thomas's results, with which we have only one energy in common.

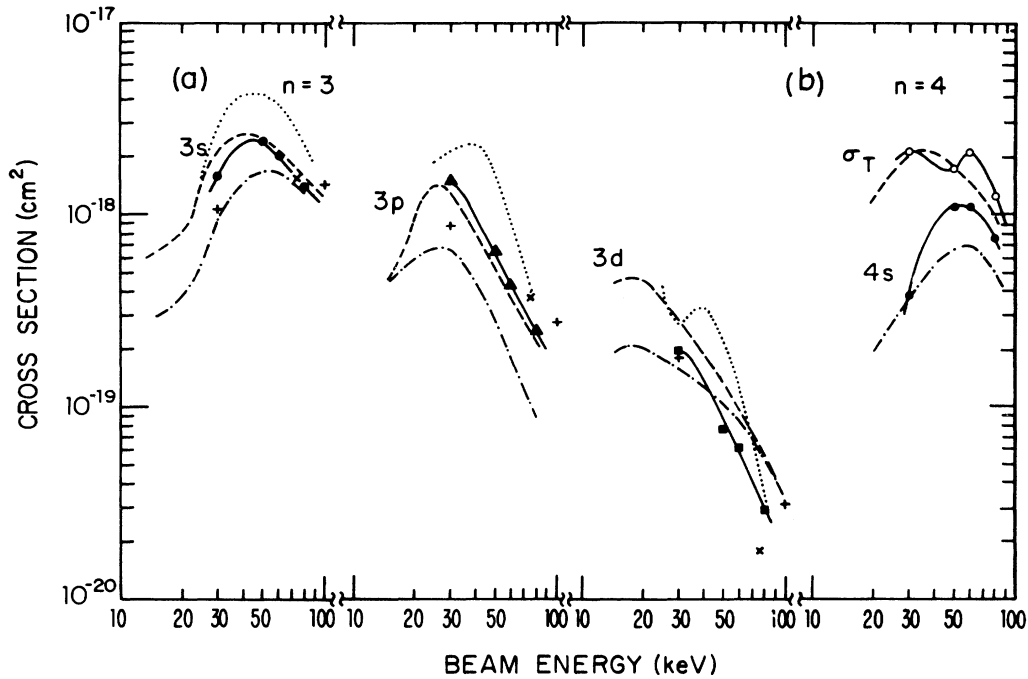


FIG. 12. (a) Results of this experiment for  $n=3$  cross sections summed over  $M_L$  together with the results of other experiments and the theoretical predictions. The solid symbols are the results of this experiment with solid curves drawn to guide the eye. The  $x$ 's are the measurements of Ford and Thomas (Ref. 14). The dashed curves are the measurements of Lenormand (Ref. 17). The dot-dash curves are the measurements of Hughes *et al.* (Ref. 12). The pluses are the theoretical predictions of Winter and Lin (Ref. 24). The dotted curve is the (AO+) calculation of Jain, Lin, and Fritsch (Ref. 27). (b) Results of this experiment for  $n=4$  cross sections together with the results of other experiments. The open and solid points are, respectively, the results of this experiment for the total cross section  $\sigma_T$  and the cross section for capture into the  $4s$  state. The solid curves are drawn through the points to guide the eye. The dashed curve is for the measurements of Lenormand (Ref. 17) for the total cross section. The dot-dash curve is for the measurements of Hughes *et al.* (Ref. 31).

Besides the difference in methods, the most important feature distinguishing our experiment from the others is the inclusion of cascades. Lenormand and Ford and Thomas conclude that cascades are unimportant from the good agreement between their data and theoretical models which allow for only the lifetimes of the  $n=3$  states. Hughes *et al.* give no indication of having considered the problem. Nevertheless, calculation shows that at distances more than 5 cm downstream of the target, cascade feeding by the  $4s$  state dominates the population of the  $3p$  state; the contribution of the  $4p$  and  $4d$  states also cannot be ignored. The other experiments all observed the radiation emitted as a function of distance along the beam line well beyond this point. Besides changing the populations of the  $n=3$  states, cascades introduce components in the radiation with the lifetimes of the higher states. It is impossible to say without detailed analysis whether excluding these lifetimes significantly affected the results of the other experiments. It is worth noting, however, that only Lenormand's experiment, which is in close agreement with ours, measured the radiation emitted inside the target and so could be expected to be the least influenced by cascades.

The atomic orbital expansion calculations of Winter and Lin,<sup>24</sup> also shown in Fig. 12, give results that appear to be somewhat higher than ours at 100 keV and somewhat lower at 30 keV. However, their relative cross sec-

tions (normalized to  $3s$ ) are almost identical to ours at both energies. Jain, Lin, and Fritsch's results<sup>27</sup> summed over  $M_L$  are significantly higher than the measured cross sections. The sharp minimum in  $\sigma_{320}$  at 30 keV is not seen experimentally.

Figure 12 compares our  $4s$  cross sections with those reported by Hughes *et al.*<sup>31</sup> in another paper. The discrepancies resemble those in the  $3s$  cross sections. However, our total  $n=4$  cross sections (summed over  $L$  and  $M_L$ ) are in good agreement with Lenormand.<sup>17</sup> Lenormand's data showed a dip near 50 keV, but it was smoothed over in the curve he drew, which is reproduced here. The dip is the result of the  $4s$  and  $4p$  cross sections reaching maxima at different energies. These two comparisons suggest that our understanding of cascades is satisfactory.

## VII. CONCLUSIONS

This experiment has measured for the first time the  $n=3, L, |M_L|$  electron-capture cross sections for protons incident on helium over a range of energies. The results reveal significant discrepancies with theory; more theoretical and experimental work is required. The results summed over  $M_L$  appear to confirm an earlier experiment by Lenormand<sup>17</sup> and cast doubt on a second, better-known experiment by Hughes *et al.*<sup>12</sup> We have es-

tablished that the microwave-resonance, optical-detection method provides a sensitive measure of the  $3p$  and  $3d$  cross sections. We have also demonstrated the importance of cascades; they should be taken into account in future experiments. We hope our results will simulate new theoretical and experimental research on this important collision process.

#### ACKNOWLEDGMENTS

We thank J. Risley, W. Westerveld, and C. C. Havener for informative discussions of their measurements and J.

Burgdörfer, L. J. Dubé, A. Jain, and T. G. Winter for sending us copies of their papers prior to publication and providing enlightenment concerning the theory. We thank Bob Landis of the RCA Corporation at Lancaster, Pennsylvania, for measuring the detection efficiency of the RCA 8852 photomultiplier tube used in the experiment. David Weitz was a great aid in taking data. This research was supported in part by the National Science Foundation under Grant Nos. PHY80-26547, PHY84-10330, and PHY-87-04527.

\*Present address: Union of Concerned Scientists, 26 Church Street, Cambridge, MA 02138.

- <sup>1</sup>R. A. Mapelton, *Theory of Charge Exchange Collisions* (Wiley-Interscience, New York, 1972).
- <sup>2</sup>E. W. Thomas, *Excitation in Heavy Particle Collisions* (Wiley, New York, 1972).
- <sup>3</sup>J. E. Bayfield, in *Atomic Physics 4*, edited by G. zu Putlitz, E. W. Weber, and A. Winnacher (Plenum, New York, 1975).
- <sup>4</sup>J. Burgdörfer, *Phys. Rev. A* **24**, 1756 (1981).
- <sup>5</sup>M. P. Silverman and F. M. Pipkin, *J. Phys. B* **7**, 704 (1974).
- <sup>6</sup>M. P. Silverman and F. M. Pipkin, *J. Phys. B* **7**, 730 (1974).
- <sup>7</sup>M. P. Silverman and F. M. Pipkin, *J. Phys. B* **7**, 747 (1974).
- <sup>8</sup>R. J. Knize, S. R. Lundeen, and F. M. Pipkin, *Phys. Rev. Lett.* **49**, 315 (1982).
- <sup>9</sup>R. J. Knize, S. R. Lundeen, and F. M. Pipkin, *Phys. Rev. A* **29**, 1114 (1984).
- <sup>10</sup>R. H. Hughes, H. R. Dawson, B. M. Doughty, D. B. Kay, and C. A. Stigers, *Phys. Rev.* **146**, 53 (1966) (5–115 keV).
- <sup>11</sup>E. P. Andreev, V. A. Ankudinov, S. B. Bobashev, and V. B. Mateev, *Zh. Eksp. Teor. Fiz.* **52**, 357 (1967) [*Sov. Phys.—JETP* **25**, 232 (1967)].
- <sup>12</sup>R. H. Hughes, C. A. Stigers, B. M. Doughty, and E. D. Stokes, *Phys. Rev. A* **1**, 1424 (1970) (10–120 keV).
- <sup>13</sup>J. L. Edwards and E. W. Thomas, *Phys. Rev. A* **2**, 2346 (1970) (75–350 keV).
- <sup>14</sup>J. C. Ford and E. W. Thomas, *Phys. Rev. A* **5**, 1694 (1972) (75–600 keV).
- <sup>15</sup>R. J. Conrads, T. W. Nichols, J. C. Ford, and E. W. Thomas, *Phys. Rev. A* **7**, 1928 (1973) (80–700 keV).
- <sup>16</sup>H. R. Dawson and D. H. Loyd, *Phys. Rev. A* **9**, 166 (1974) (1.2–8.2 keV).
- <sup>17</sup>J. Lenormand, *J. Phys. (Paris)* **37**, 699 (1976) (15–80 keV).
- <sup>18</sup>H. R. Dawson and D. H. Loyd, *Phys. Rev. A* **15**, 43 (1977) (3.2–8.2 keV).
- <sup>19</sup>J. S. Risley, F. J. de Meer, and C. B. Kerkijk, *J. Phys. B* **11**, 1759 (1978) (2–15 keV).
- <sup>20</sup>C. C. Havener, W. G. Westerveld, J. S. Risley, N. H. Tolk, and J. C. Tully, *Phys. Rev. Lett.* **48**, 926 (1982).
- <sup>21</sup>C. C. Havener, N. Rouze, W. B. Westerveld, and J. S. Risley, *Phys. Rev. Lett.* **53**, 1049 (1984).
- <sup>22</sup>C. C. Havener, N. Rouze, W. B. Westerveld, and J. S. Risley, *Phys. Rev. A* **33**, 276 (1986).
- <sup>23</sup>W. B. Westerveld, J. R. Ashburn, R. A. Cline, C. D. Stone, P. J. M. van der Burgt, and J. S. Risley, *Nucl. Instrum. Methods Phys. Res. B* **24**, 224 (1987).
- <sup>24</sup>T. G. Winter and C. C. Lin, *Phys. Rev. A* **10**, 2141 (1974).
- <sup>25</sup>J. Burgdörfer and L. J. Dubé, *Phys. Rev. Lett.* **52**, 2225 (1984).
- <sup>26</sup>A. Jain, C. D. Lin, and W. Fritsch, *Phys. Rev. A* **35**, 3180 (1987).
- <sup>27</sup>A. Jain, C. D. Lin, and W. Fritsch, *Phys. Rev. A* **36**, 2041 (1987).
- <sup>28</sup>A. R. Edmonds, *Angular Momentum in Quantum Mechanics* (Princeton University Press, Princeton, NJ, 1974).
- <sup>29</sup>H. A. Bethe and E. E. Salpeter, *Quantum Mechanics of One- and Two-Electron Atoms* (Plenum, New York, 1977).
- <sup>30</sup>S. K. Allison, *Rev. Mod. Phys.* **30**, 1137 (1958).
- <sup>31</sup>R. H. Hughes, H. R. Dawson, and B. M. Doughty, *Phys. Rev.* **164**, 166 (1967).